



HAL
open science

A generalized differential image motion monitor

E. Aristidi, A. Ziad, J. Chabé, Y. Fanteï-Caujolle, Cédric Renaud, C. Giordano

► **To cite this version:**

E. Aristidi, A. Ziad, J. Chabé, Y. Fanteï-Caujolle, Cédric Renaud, et al.. A generalized differential image motion monitor. *Monthly Notices of the Royal Astronomical Society*, 2019, 486 (1), pp.915-925. 10.1093/mnras/stz854 . hal-02283284

HAL Id: hal-02283284

<https://hal.science/hal-02283284>

Submitted on 30 May 2023

HAL is a multi-disciplinary open access archive for the deposit and dissemination of scientific research documents, whether they are published or not. The documents may come from teaching and research institutions in France or abroad, or from public or private research centers.

L'archive ouverte pluridisciplinaire **HAL**, est destinée au dépôt et à la diffusion de documents scientifiques de niveau recherche, publiés ou non, émanant des établissements d'enseignement et de recherche français ou étrangers, des laboratoires publics ou privés.

A generalized differential image motion monitor

E. Aristidi,¹★ A. Ziad,¹ J. Chabé,² Y. Fantéi-Caujolle,¹ C. Renaud¹ and C. Giordano¹

¹Université Côte d'Azur, Observatoire de la Côte d'Azur, CNRS, Laboratoire Lagrange, Parc Valrose, F-06108 Nice Cedex 2, France

²Université Côte d'Azur, OCA, CNRS, IRD, Géoazur, 2130 route de l'Observatoire, 06460 Caussols, France

Accepted 2019 March 18. Received 2019 March 7; in original form 2018 December 12

ABSTRACT

We present a generalized differential image motion monitor (GDIMM). It is a compact instrument dedicated to the measurement of four parameters of optical turbulence: seeing, isoplanatic angle, coherence time and wavefront coherence outer scale. The GDIMM is based on a small telescope (28 cm diameter) equipped with a three-hole mask at its entrance pupil. The instrument is fully automatic, and performs continuous monitoring of turbulence parameters at the Calern Observatory (France). This paper gives a description of the instrument, data processing and error budget. We also present statistics of three and a half years of monitoring of turbulence parameters above the Calern Observatory.

Key words: instrumentation: high angular resolution – atmospheric effects – site-testing .

1 INTRODUCTION

Atmospheric turbulence is responsible for the degradation of astronomical images observed through the atmosphere. Since the early 1970s, many techniques have been developed to achieve diffraction-limited resolution of observing instruments, namely speckle interferometry (Labeyrie 1970), long-baseline interferometry (Labeyrie 1975) and adaptive optics (Rousset et al. 1990). The performance of these techniques relies on good knowledge of atmospheric turbulence parameters, i.e. the seeing ϵ_0 , the isoplanatic angle θ_0 , the coherence time τ_0 and the outer scale \mathcal{L}_0 .

The three parameters ϵ_0 , θ_0 and τ_0 are of fundamental importance for adaptive optics (AO) correction: a large coherence time reduces the delay error, a small seeing value allows the loop to be closed easily and benefits from a rather good correction, and a large isoplanatic angle reduces the anisoplanatic error, enlarges the sky coverage and allows very wide fields of correction (see Carbillot et al. 2017 and references therein). The outer scale \mathcal{L}_0 has a significant effect for large-diameter telescopes (8 m and above) and impacts low Zernike modes such as tip-tilt (Winker 1991).

For several years, our group has been developing original techniques and instrumentation for measuring the optical turbulence of the atmosphere. Several prototypes have been developed in the past, such as the generalized seeing monitor (GSM, Ziad et al. 2000), which has become a reference for monitoring the coherence parameters of the wavefront at ground level. Over the last 15 years the GSM has been used in a large number of astronomical observatories and for prospecting potential new sites (see Ziad et al. 2000 and references therein).

The generalized differential image motion monitor (GDIMM) was proposed in 2014 (Aristidi et al. 2014) to replace the aging GSM. It is a compact instrument very similar to a DIMM (Sarazin & Roddier 1990), with three sub-apertures of different diameters. The GDIMM observes bright single stars up to magnitude $V \sim 2$, at zenith distances up to 30° , which is enough to ensure observability at any time or night of the year.

After a period of development and tests in 2013–2015, the GDIMM has been operational since the end of 2015, as a part of the Calern Atmospheric Turbulence Station (CATS) (Côte d'Azur Observatory – Calern site, France, UAI code: 010, latitude $43^\circ 45' 13''$ N, longitude $06^\circ 55' 22''$ E). The GDIMM provides continuous monitoring of four turbulence parameters (ϵ_0 , θ_0 , τ_0 and \mathcal{L}_0) above the Calern Observatory. Data are displayed in real time through a website (cats.oca.eu), the idea being to provide a service available to all observers at Calern, as well as building a database to make long-term statistics of turbulence (before CATS, no such database existed for this site, despite its 40 years of activity as an astronomical site). The other objective is for Calern to become an operational on-sky test platform for the validation of new concepts and components in order to overcome current limitations of high angular resolution (HRA) existing systems. Several activities regarding adaptive optics are operated at the MéO (Samain et al. 2008) and C2PU (Bendjoya et al. 2012) telescopes and they benefit from the data given by the CATS station.

This paper is organized as follows: Section 2 describes the instrument. Sections 3 to 6 present the method used to derive each parameter (seeing, isoplanatic angle, coherence time and outer scale) and the associated error budget. Section 7 is devoted to results obtained at the Calern observatory. A final discussion is presented in Section 8.

* E-mail: Eric.Aristidi@unice.fr

2 INSTRUMENT DESCRIPTION

The GDIMM is based on a commercial Celestron C11 telescope (diameter 28 cm), driven by an equatorial mount Astro-Physics AP900, controlled remotely by a computer. It is equipped with a pupil mask made of three sub-pupils (Fig. 1, left). Two sub-pupils are circular with a diameter $D_1 = 6$ cm, separated by a distance $B = 20$ cm along the declination axis. Both are equipped with a glass prism oriented to give opposite tilts to the incident light. The third sub-aperture is circular, with diameter $D_3 = 10$ cm and a central obstruction of 4 cm and was designed to estimate the isoplanatic angle. It is protected by a glass parallel plate. A wide-field finder with a webcam is used to point to stars and centre them on the telescope.

The main camera is a Prosilica EC650. It offers good sensitivity in the visible domain with a peak near the wavelength $\lambda = 500$ nm. The pixel size is $7.4 \mu\text{m}$. A Barlow lens enlarges the telescope focal to meet sampling requirements (we have $\lambda/D_1 = 7$ pixels and $\lambda/D_3 = 4$ pixels for $\lambda = 500$ nm). The camera allows short exposure times and region-of-interest (ROI) definition to increase the frame rate. An exposure time of a few milliseconds is required to observe stars of magnitude $V < 2$ with sufficient signal-to-noise ratio (SNR). The frame rate is limited by the hardware; it is about 100 frames per second for our observations. Such a high cadence is mandatory to properly sample the temporal variability of angles of arrival (AA) and to estimate the coherence time (see Section 5.2).

An example of a GDIMM short-exposure image is shown on Fig. 2. It was obtained at Calern Observatory on 2018 April 4 at 20:55 UT on the star Regulus (α Leo, magnitude $V = 1.4$). The exposure time was 10 ms for this image. The central spot corresponds to sub-pupil 3 (diameter 10 cm); it is brighter than the other two, as expected. The first Airy ring is visible around the central spot: the seeing was $\epsilon_0 = 1.3$ arcsec for the wavelength $\lambda = 500$ nm (Fried diameter $r_0 = 8$ cm, close to the pupil diameter). The image quality can be checked by computing the Strehl ratio of sub-images, using a simple formula proposed by Tokovinin (2002). It is generally assumed that image quality is good when the Strehl ratio is over 30 per cent (this corresponds to phase distortions lower than $\lambda/5$ over the pupil surface). For this example the three Strehl ratios are 0.79, 0.83 and 0.36 for spots corresponding to sub-pupils 1, 2 and 3.

The acquisition software is written in C++/QT. It drives the whole observing sequence: dome opening, choice of target star, telescope pointing, image acquisition, computation of turbulence parameters. The instrument is now fully automatic. It uses information from a meteorological station and an all-sky camera to check observability. Observations are stopped if conditions deteriorate.

The GDIMM is placed on the top of a 4 m high concrete pillar, and protected by an all-sky dome (Fig. 1, right). A more detailed description is given in previous papers (Aristidi et al. 2014; Ziad et al. 2017; Ziad et al. 2018b; Aristidi et al. 2018).

2.1 Data processing

GDIMM data are based on sequences of two successive sets of $N = 1024$ frames of a bright star, taken at exposure times $T = 5$ ms and $2T = 10$ ms. The full image size is 659×493 pixels. Every frame contains three sub-images of the star, corresponding to the three sub-pupils of the instrument (see Fig. 2). Images are cropped in a rectangular zone (the ROI) of size 380×150 pixels containing the three stellar spots. This allows a cadence of 100 frames per second to be attained. After sky background removal and thresholding, we

calculate the three photocentres and integrated intensities. These raw data are logged into a file for optional further processing. A series of filters is then applied to control the data quality:

(i) Sub-image detection is made in three square boxes (size 30×30 pixels for lateral spots corresponding to pupils 1 and 2, 45×45 pixels for the central spot, pupil 3) whose position is calculated on the first frame of the sequence. Sub-images for which the photocentre is too close to the box edge are rejected (this happens in cases of strong wind or mount drift).

(ii) Outlier detection and rejection is made on photocentre coordinates and intensities.

(iii) Sub-images corresponding to pupil 3 (diameter $D_3 = 10$ cm) must be brighter than sub-images of pupils 1 and 2 (diameter $D_1 = 6$ cm). They are rejected if this is not the case.

(iv) Drift correction is applied by removing a linear trend on photocentre time series.

The four turbulence parameters are then calculated (a detailed description is given hereafter). The whole process (acquisition + processing) takes less than one minute. The GDIMM provides one set of turbulence parameters every 2 min; they are sent to a database for real-time display on the CATS website (cats.oca.eu). Note that there is some dead time between two successive acquisitions to match this cadence of 2 min. We made this choice regarding the characteristic time of evolution of parameters, which is a few minutes (see Ziad 2016 and references therein). If we suppress the dead time, we can have a parameter quadruplet per minute with our current hardware. Some tests are currently being made to see if the parameter stability can be improved, especially for the outer-scale estimation.

3 SEEING MEASUREMENTS

3.1 Theory

Seeing estimations by the GDIMM are based on differential motion. The principle of seeing estimation is well known (Sarazin & Roddier 1990). It is based on variances of the photocentre difference of images produced by sub-pupils 1 and 2 (Fig. 1, left). The seeing ϵ_0 (in radians) is computed using the following formulae (Tokovinin 2002):

$$\epsilon_{0,||t} = 0.98 \left(\frac{D}{\lambda} \right)^{0.2} \left(\frac{\sigma_{||t}^2}{K_{||t}} \right)^{0.6} \quad (1)$$

with

$$\begin{aligned} K_1 &= 0.364 (1 - 0.532b^{-1/3}) \\ K_t &= 0.364 (1 - 0.798b^{-1/3}) \end{aligned} \quad (2)$$

where B is the distance between the sub-apertures, D their diameter, $b = B/D$, and λ the wavelength, traditionally set to 500 nm as a standard. $\sigma_{||t}^2$ are the longitudinal and transverse differential variances, calculated at the zenith (the correction is $\sigma^2(z=0) = \sigma^2(z) \cos(z)$ with z the zenithal angle). Two estimations of the seeing are obtained for a given sequence; they are supposed to be almost identical (isotropic hypothesis) and are averaged.

Differential variances (longitudinal and transverse) $\sigma_{||t,T}^2$ and $\sigma_{||t,2T}^2$ are calculated for sets corresponding to exposure times T and $2T$. They are compensated from the finite exposure T time using an exponential interpolation as proposed by Tokovinin (2002):

$$\sigma_{||t}^2 = (\sigma_{||t,T}^2)^n (\sigma_{||t,2T}^2)^{1-n}. \quad (3)$$

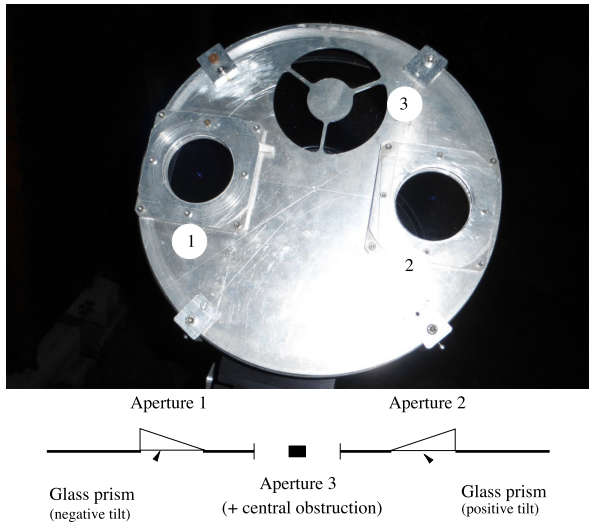


Figure 1. Left: the pupil mask of the GDIMM (bottom part is a sectional view). Right: the GDIMM dome on its 4 m high tower at Calern Observatory.

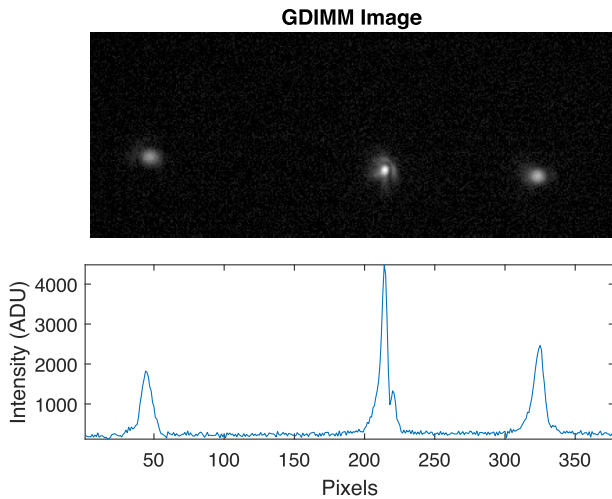


Figure 2. Top: GDIMM instantaneous image, taken on 2018 April 4, 20:55 UT, of the star Regulus (α Leo) with an exposure time of 10 ms. Bottom: 1D projection of the image (sum of lines).

This correction increase variances by a factor of the order of 10–20 per cent. Two values of the seeing $\epsilon_{0,lt}$ are deduced from equation (1) and averaged.

3.2 Error analysis

3.2.1 Statistical error

The variance of image motion at exposure times T and $2T$ is computed from samples of $N = 1024$ individual frames: they are then affected by statistical noise due to the finite size of the sample. Assuming statistical independence between the frames, the statistical error on the variance σ^2 (both at exposure times T and $2T$) is given by (Frieden 1983)

$$\frac{\delta\sigma^2}{\sigma^2} = \sqrt{\frac{2}{N-1}}, \quad (4)$$

which propagates on to the seeing an error contribution $\delta\epsilon_0$. With 1024 independent frames we have $\frac{\delta\sigma^2}{\sigma^2} = 4.4$ per cent. The error on the seeing is calculated from equations (1) and (3) and gives $\frac{\delta\epsilon_0}{\epsilon_0} \simeq 5$ per cent. This is the main source of uncertainty in our seeing estimations.

3.2.2 Scale error

Differential variances are obtained in units of square pixels and require calibration of the pixel size. This is done by making image sequences of the binary star β Cyg AB (separation 34.6 arcsec). We measured a pixel scale of $\xi = 0.242 \pm 0.003$ arcsec.

The uncertainty on ξ propagates into the differential variances when the conversion from pixels into arcsec is performed. It gives a relative contribution on the differential variances $\frac{\delta\sigma^2}{\sigma^2} = 0.6$ per cent and on the seeing $\frac{\delta\epsilon_0}{\epsilon_0} = 0.4$ per cent.

The scale calibration has to be done regularly: the telescope tube is subject to thermal dilatations that result in slight variations δF of the focal length F , especially during the transition between the summer and the winter. We measured relative variations $\frac{\delta F}{F} \lesssim 1$ per cent, leading to a relative uncertainty $\frac{\delta\epsilon_0}{\epsilon_0} \simeq 1$ per cent on the seeing. This remains lower than the statistical error.

3.2.3 Background noise

The sky background is an additive Poisson noise independent of the stellar signal. Its influence on DIMM data is discussed in Tokovinin (2002). It biases the computed differential variances by a term

$$\sigma_B^2 = 2 \frac{B^2}{I^2} \sum_{\text{window}} (x_{ij} - \bar{x})^2 \quad (5)$$

where I is the total stellar flux, B is the sky background standard deviation and x_{ij} the coordinates of contributing pixels (the number of illuminated pixels in the star image is typically of the order of 300 after thresholding and that defines the ‘window’ over which the summation is made). With our data, the bias term is $\sigma_B^2 \simeq 10^{-2}$ pixel², giving a relative error $\frac{\delta\sigma^2}{\sigma^2} = 0.2$ per cent. This is negligible compared to the statistical error.

Other instrumental noises include the readout noise of the CCD, and the error on the centroid determination. These errors have been studied in detail in the past (see Ziad et al. 1994 and references therein) and have a very small contribution, orders of magnitude below the statistical error.

4 ISOPLANATIC ANGLE MEASUREMENTS

4.1 Theory

The isoplanatic angle θ_0 is estimated from the scintillation of a single star observed through sub-pupil 3, with a diameter of 10 cm and a central obstruction of 4 cm (Fig. 1, left). The scintillation index is the ratio of the variance σ_I^2 of the stellar intensity, divided by the square of its mean value \bar{I} :

$$s = \frac{\sigma_I^2}{\bar{I}^2}. \quad (6)$$

The principle of the calculation is based on the similarity of the theoretical expressions of θ_0 and the scintillation index s (Loos & Hogge 1979; Ziad et al. 2000). θ_0 is obtained (in arcsec) for a wavelength $\lambda = 500$ nm by the following formula:

$$\theta_0^{-5/3} = A s \quad (7)$$

where $A = 14.87$ is computed numerically from equations (19) and (21) of Ziad et al. (2000) using the value $h_0 = 10$ km. The scintillation index s is corrected from the zenithal distance z by the formula $s(z = 0) = s(z) \cos(z)^{8/3}$.

Simultaneous measurements of the seeing and the isoplanatic angle make it possible to derive the equivalent turbulence altitude defined by Roddier, Gilli & Vernin (1982) as

$$\bar{h} = 0.31 \frac{r_0}{\theta_0} \quad (8)$$

with $r_0 = 0.98 \frac{\lambda}{\epsilon_0}$ the Fried parameter. Statistics for \bar{h} at Calern are presented in Section 7.

4.2 Isoplanatic angle estimation

Scintillation indexes (sub-image corresponding to pupil 3) s_T and s_{2T} are calculated for sets corresponding to exposure times T and $2T$. These sets are composed of $N = 1024$ images, representing about 10 s of data. This integration time appears to be long enough for the scintillation index to converge. To check this, we recorded long data sequences (up to 4000) of images and calculated the scintillation index for integration times varying from 0 to 40 s. The result is shown in Fig. 3 for three different sets taken at Calern on the night of 2018 March 19. Scintillation indexes show satisfactory convergence (below 2 per cent) after 10 s of integration time.

Compensation from the finite exposure time is made by linear extrapolation on scintillation indexes as proposed by Ziad et al. (2000):

$$s = 2s_T - s_{2T}. \quad (9)$$

This compensation is more critical on the scintillation than on the differential variances. The correction can be of the order of 30–50 per cent. The isoplanatic angle is then derived from equation (7).

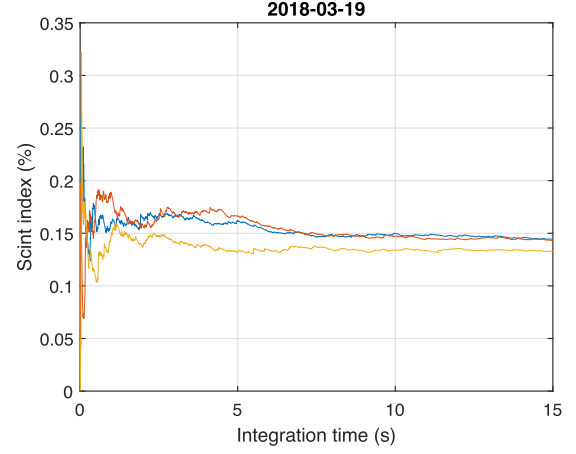


Figure 3. Scintillation index as a function of the integration time for three different data sets taken at Calern on the night of 2018 March 19. The horizontal axis is limited to the range 0–15 s.

4.3 Error analysis

4.3.1 Statistical error

The isoplanatic angle is estimated from the scintillation index s via equation (6). Two estimates s_T and s_{2T} are made, corresponding to exposure times T and $2T$, and combined to obtain the scintillation index corrected from the exposure time effects (equation 9). The error on s_T (as for s_{2T}) is

$$\frac{\delta s_T}{s_T} = \frac{\delta \sigma_I^2}{\sigma_I^2} + 2 \frac{\delta \bar{I}}{\bar{I}}. \quad (10)$$

If we assume statistical independence between frames, the first term is the same as that for the seeing and the second is $\frac{2}{\sqrt{N}}$. We get

$$\frac{\delta s_T}{s_T} = \sqrt{\frac{2}{N-1}} + \frac{2}{\sqrt{N}} \simeq 10 \text{ per cent.} \quad (11)$$

However, in cases of slow wind speed in the upper atmosphere (the major contributor to scintillation) the number of independent frames within an image cube is reduced to a number $N_I < N$ and we must replace N by N_I in the previous equation. An order of magnitude of N_I is given by the ratio

$$N_I = \frac{N t_e}{D_3/v} \quad (12)$$

where D_3 is the diameter of the sub-pupil 3, $N t_e$ the integration time (10 s at a frame rate of 100 Hz) and v the wind speed of atmospheric layers contributing to the scintillation (high altitude layers). We do not know v , but we can have its order of magnitude by looking at the distribution of the effective wind speed \bar{v} defined in equation (16). At Calern observatory, the distribution is bimodal (as shown in Fig. 11) and high layers have a speed of the order of 13 m s^{-1} . Taking this value for v , we obtain $N_I \simeq 1300$, which is the same order of magnitude as the number N of frames in a data cube. Using equation (9), we obtain the relative statistical error on the zero exposure time scintillation index:

$$\frac{\delta s}{s} \simeq 15 \text{ per cent.} \quad (13)$$

There is another error source depending on the constant A in equation (7). A is indeed a function of an altitude parameter h_0 defined in equation (21) of Ziad et al. (2000). The relation $A(h_0)$ is a function of the pupil geometry and is analytic. Its dependence on

h_0 remains weak; we found the relative error

$$\frac{\delta A}{A} \lesssim 5 \text{ per cent} \quad (14)$$

in the range $h_0 \in [1, 25]$ km. The relative statistical error on the isoplanatic angle is

$$\frac{\delta \theta_0}{\theta_0} = \frac{3}{5} \frac{\delta A}{A} + \frac{3}{5} \frac{\delta s}{s} \simeq 15 \text{ per cent.} \quad (15)$$

4.3.2 Sky background

The presence of a sky background on individual images introduces a bias on the estimation of the mean stellar intensity \bar{I} , its standard deviation σ_I and then on the scintillation index s . The observed background on our images is typically 40 ADU pixel⁻¹. Its relative contribution to the stellar flux (integrated on the star image) represents about 30 per cent for bright stars such as Deneb (α Cyg, magnitude $V = 1.2$) observed by the GDIMM. To estimate the bias, let us introduce the following variables:

(i) B , the background intensity collected over the N_I pixels illuminated by the star after threshold application, \bar{B} and σ_B^2 its mean and variance. B is a Poisson random variable; it must satisfy $\sigma_B = \sqrt{\bar{B}}$, which has been well verified on images.

(ii) I , the total intensity (background + stellar flux) collected over the N_I pixels.

The stellar flux is given by $I = I_r - B$, the measure being I_r . The mean \bar{I} is biased by the term \bar{B} . This bias is estimated and removed as indicated above, but the background fluctuations lead to an error δI on the estimation of \bar{I} equal to $\delta I = \sigma_B \simeq \sqrt{\bar{B}}$. Similarly, the intensity variance σ_I^2 is biased by a term σ_B^2 .

The error on the scintillation index is calculated from equation (10) taking $\delta \sigma_I^2 = \sigma_B^2$ (bias on intensity variance) and $\delta \bar{I} = \sigma_B$. Typical values are, in ADU: $\sigma_B \simeq 240$, $\bar{I} \simeq 100\,000$, $\sigma_I \simeq 30\,000$. That gives a background error on the scintillation index $\frac{\delta s}{s} \leq 1$ per cent, which is an order of magnitude below the statistical error.

5 COHERENCE TIME MEASUREMENTS

5.1 Theory

The coherence time τ_0 relevant for AO applications is defined by Roddier (1981):

$$\tau_0 = 0.31 \frac{r_0}{\bar{v}} \quad (16)$$

where \bar{v} , the effective wind speed, is a weighted average of the wind speed on the whole atmosphere. It can be estimated (Ziad et al. 2012; Aristidi et al. 2014; Ziad et al. 2017) from the temporal structure functions $D_{x|y}(\tau)$ of the AA in the x (resp. y) direction (parallel to the declination (resp. right ascension)). This function is zero for $\tau = 0$ and saturates to a value D_s for large τ , and its characteristic time

$$D(\tau_{AA,x|y}) = \frac{D_s}{e} \quad (17)$$

defines the decorrelation time of AA fluctuations in directions x and y . To calculate the effective wind speed \bar{v} , we make use of the work by Conan et al. (2000) and Ziad et al. (2012) who gave two approximations of \bar{v} (in m s⁻¹) corresponding to two different regimes:

(i) For $\tau_{AA,x|y} > \frac{D}{\bar{v}}$:

$$\bar{v} = 10^3 D G^{-3} \left[\tau_{AA,x}^{\frac{1}{3}} + \tau_{AA,y}^{\frac{1}{3}} \right]^{-3} \quad (18)$$

where D is the sub-pupil diameter and G a constant (Conan et al. 2000):

$$G = \frac{(1-e^{-1})(3.001 K^{\frac{1}{3}} + 1.286 K^{\frac{2}{3}}) + e^{-1}(2.882 + 1.628 K^2)}{0.411 + 0.188 K^2} \quad (19)$$

with $K = \frac{\pi D}{\lambda_0}$. This case is met almost all the time with small pupils like the GDIMM ones.

(ii) For $\tau_{AA,x|y} < \frac{D}{\bar{v}}$ (this case was never observed with our data):

$$\bar{v} = \frac{D \sqrt{G_1}}{2} \left[\tau_{AA,x}^{-2} + \tau_{AA,y}^{-2} \right]^{\frac{1}{2}} \quad (20)$$

with

$$G_1 = \frac{2.62}{e} \left(1 - 1.04 K^{\frac{1}{3}} + 0.57 K^2 - 0.45 K^{7/3} \right). \quad (21)$$

We obtain three values of \bar{v} for the three sub-pupils, which are averaged. The coherence time τ_0 is eventually calculated from r_0 and \bar{v} using equation (16).

5.2 Coherence time estimation

We remarked that the frame rate (100 frame s⁻¹) is slightly variable: the first operation is then to resample time series of photocentre coordinates with a constant time step δt (after some trials, we chose $\delta t = 5$ ms). 12 structure functions $D(\tau)$ are computed for the 12 photocentre series (two coordinates for three sub-images, and two frame sets for exposure times T and $2T$) using the direct expression

$$D_{x|y}(\tau) = \langle [x|y(t) - x|y(t + \tau)]^2 \rangle \quad (22)$$

where $\langle \rangle$ stands for ensemble average over the $N = 1024$ frames. Structure functions are compensated from a finite exposure time using the same method as for the seeing:

$$D_{x|y}(\tau) = D_{x|y,T}(\tau)^n D_{x|y,2T}(\tau)^{1-n} \quad (23)$$

where $D_{x|y,T}$ and $D_{x|y,2T}$ are calculated on image cubes taken with exposure times of T and $2T$, and $n = 1.75$. An example of structure functions is shown in Fig. 4. Curves correspond to the x -axis (declination) and are divided by their respective saturation value D_s . One can see that saturation is attained after 0.3–0.4s, and that there are some fluctuations of $D_x(\tau)$ in the saturation regime. These fluctuations are the main source of uncertainty in the determination of τ_{AA} , as discussed in Section 5.3. The graph on the right is an enlargement for small values of τ : curves intersect with the line $\frac{D_x(\tau)}{D_s} = \frac{1}{e}$ at $\tau_{AA,1} = 9.5$ ms, $\tau_{AA,2} = 8.8$ ms and $\tau_{AA,3} = 6.1$ ms.

For each sub-pupil, the effective wind speed \bar{v} is calculated from equation (18). The three values of \bar{v} are then averaged.

5.3 Error analysis

The coherence time is deduced from the AA decorrelation time τ_{AA} defined by equation (17). To calculate the error on τ_{AA} , we express the finite difference

$$\delta D_0(\tau) \simeq D'_0(\tau) \delta \tau \quad (24)$$

where $D_0(\tau) = \frac{D(\tau)}{e}$ is the normalized structure function and $D'_0(\tau)$ the derivative of D_0 . Then, it is possible to estimate the error $\delta \tau$ at

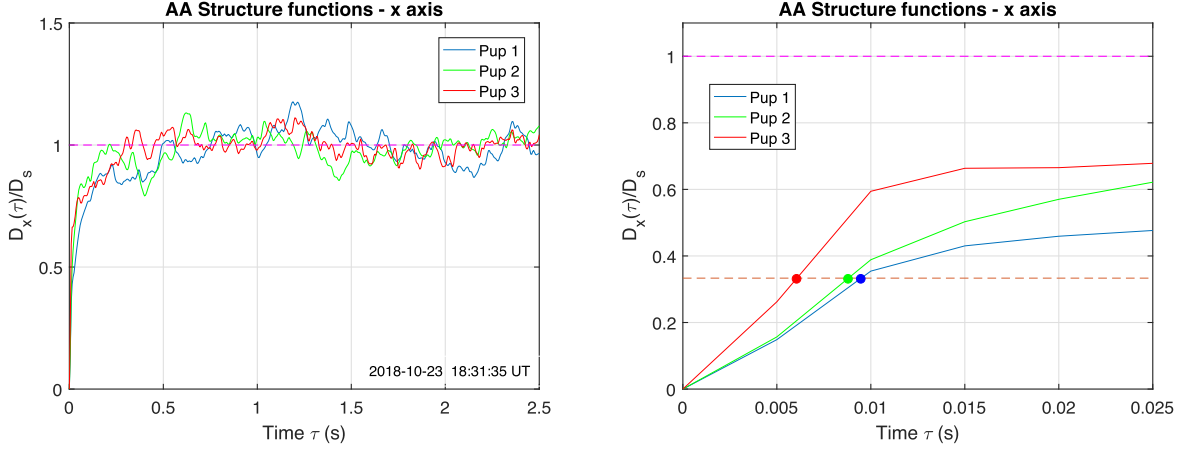


Figure 4. Example of normalized structure functions of AA fluctuations along the x -axis, calculated for the three sub-pupils (and compensated from exposure time). Left: structure functions $\frac{D_x(\tau)}{D_s}$ divided by their saturation value. Right: enlargement for $\tau \in [0, 25]$ ms. The three curves intersect the line $\frac{D_x(\tau)}{D_s} = \frac{1}{e}$ (brown dashed line) at $\tau = \tau_{AA}$ (circles).

Table 1. Relative errors on the estimation of the AA decorrelation time for the three sub-pupils and the two directions.

	sub-pup. 1		sub-pup. 2		sub-pup. 3	
	x	y	x	y	x	y
$\frac{\Delta\tau}{\tau_{AA}}$	29%	35%	29%	37%	27%	27%

$\tau = \tau_{AA}$:

$$\delta\tau = \frac{\Delta D_0}{D'_0(\tau_{AA})}. \quad (25)$$

The error on D_0 can be estimated as the standard deviation of the structure function in the saturation zone; typical values are 10 per cent to 20 per cent. The derivative $D'_0(\tau_{AA})$ can be estimated by the slope of the structure function at $\tau = \tau_{AA}$. Errors on τ_{AA} were calculated for each of the six structure functions, for a three-month data sample. We found a typical error of ~ 30 per cent. Relative errors on $\tau_{AA, x/y}$ for each sub-pupil are summarized in Table 1.

The error on τ_{AA} propagates to the effective wind speed, giving a contribution $\delta_{v, \tau}$ to the uncertainty on \bar{v} , obtained by differentiation of equation (18). For a relative error of 30 per cent on τ_{AA} , this contribution $\delta_{v, \tau}$ is of 10 per cent (for $\tau_{AA} = 6$ ms) to 20 per cent (for $\tau_{AA} = 24$ ms).

In addition, the effective wind speed \bar{v} calculated from equation (18) needs an estimate of the outer scale \mathcal{L}_0 . However, as discussed in Section 6.3, the outer scale is strongly filtered and a measurement is not always available. In this case the standard value $\mathcal{L}_0 = 20$ m is used. This results in a bias $\delta_{v, L}$ on the effective wind speed. This bias remains below 20 per cent for outer scales $\mathcal{L}_0 \in [10, 40]$ m, which covers the majority of the situations on traditional sites. Combining these two contributions, the relative uncertainty on \bar{v} is then $\frac{\delta_{\bar{v}}}{\bar{v}} \simeq 20$ per cent to 30 per cent.

The error δ_{τ_0} on the coherence time τ_0 is obtained from equation (16):

$$\frac{\delta_{\tau_0}}{\tau_0} = \frac{\delta_{\epsilon_0}}{\epsilon_0} + \frac{\delta_{\bar{v}}}{\bar{v}} \simeq 25 \text{ per cent to } 35 \text{ per cent.} \quad (26)$$

6 OUTER-SCALE MEASUREMENTS

6.1 Theory

The outer scale is, among the four turbulence parameters measured by the GDIMM, the most difficult to estimate with a small instrument. In previous papers (Ziad et al. 1994; Aristidi et al. 2014) we proposed to make use of variances of the absolute motions of sub-images to estimate the outer scale \mathcal{L}_0 . These absolute variances (in square radians) are given by (Ziad et al. 1994)

$$\sigma_D^2 = 0.17 \lambda^2 r_0^{-5/3} (D^{-1/3} - 1.525 \mathcal{L}_0^{-1/3}). \quad (27)$$

Because of telescope vibrations, direct estimation of \mathcal{L}_0 from absolute variances using equation (27) is not reliable. Our first idea, following the work by Ziad et al. (1994), was to use the inverse relative difference of variances measured with sub-pupils 1 (or 2) and 3 (diameters 6 cm and 10 cm), i.e.

$$R = \frac{\sigma_{D_1}^2}{\sigma_{D_3}^2} = \frac{D_1^{-1/3} - 1.525 \mathcal{L}_0^{-1/3}}{D_3^{-1/3} - 1.525 \mathcal{L}_0^{-1/3}}. \quad (28)$$

But with our values for D_1 and D_3 , the variation is weak for decametric values of \mathcal{L}_0 , as illustrated by Fig. 5 and Table 2. We have $1/R = 0.216$ for $\mathcal{L}_0 = 10$ m and 0.200 for $\mathcal{L}_0 = 20$ m. To extract reliable \mathcal{L}_0 from this estimator, we need high precision on variances (about 1 per cent), which is not the case (the statistical error on variances is of the order of 5 per cent, as discussed in Section 3.2, and there is some bias from telescope vibration).

We then looked for another estimator for \mathcal{L}_0 , and found that it was possible to use the ratio of absolute to differential variances of image motion:

$$Q_i = \frac{\sigma_{D_i}^2}{\sigma_{\parallel i}^2} \quad (29)$$

where $\sigma_{D_i}^2$ is the absolute variance corresponding to the sub-pupil i , and $\sigma_{\parallel i}^2$ the longitudinal or transverse differential variance used to calculate the seeing (equation 1). This gives two expressions for

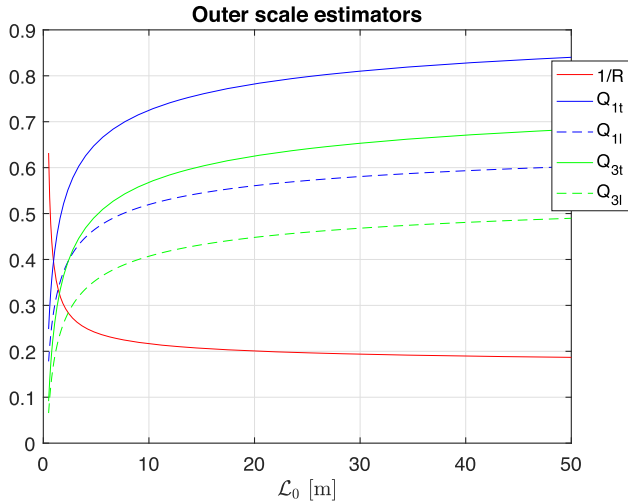


Figure 5. Outer-scale estimators: $1/R$ (equation 28) and $Q_{i,|t}$ (equation 30) as a function of \mathcal{L}_0 .

Table 2. Value of ratios $1/R$ (equation 28) and $Q_{i,|t}$ (equation 30) for $\mathcal{L}_0 = 10$ m and $\mathcal{L}_0 = 20$ m. Column 4 is the required precision on variances to discriminate between the two values of \mathcal{L}_0 .

	$\mathcal{L}_0 = 10$ m	$\mathcal{L}_0 = 20$ m	Required precision on variances
$1/R$	0.216	0.200	1%
$Q_{1, t}$	0.520	0.560	4%
$Q_{1,t}$	0.725	0.782	4%
$Q_{3, t}$	0.407	0.448	5%
$Q_{3,t}$	0.578	0.625	5%

the ratios Q_i :

$$Q_{i,|t} = \frac{\sigma_{D_i}^2}{\sigma_t^2} = 0.17 \frac{D_i^{-1/3} - 1.525\mathcal{L}_0^{-1/3}}{0.364D_1^{-1/3} - 0.2905B^{-1/3}}$$

$$Q_{i,t} = \frac{\sigma_{D_i}^2}{\sigma_1^2} = 0.17 \frac{D_i^{-1/3} - 1.525\mathcal{L}_0^{-1/3}}{0.364D_1^{-1/3} - 0.1904B^{-1/3}}. \quad (30)$$

Using absolute variances from the three sub-pupils, we get six estimations of \mathcal{L}_0 , from which we take the median value. Note that the absolute variance at the numerator of equation (29) may be contaminated by telescope vibrations. Hence we use only the x direction (declination axis) to compute absolute variances to reduce oscillations from the motor of the mount. Fig. 5 shows the variation of ratios $1/R$ and $Q_{i,|t}$ as a function of \mathcal{L}_0 . All estimators have weak dependence with decametric \mathcal{L}_0 , but the ratios Q_i are a little more sensitive. In Table 2 we computed the expected Q_i ratios for $\mathcal{L}_0 = 10$ m and $\mathcal{L}_0 = 20$ m, and the required precision on variances to discriminate between the two values of \mathcal{L}_0 . We found that this required precision is 4–5 percent for the ratios Q_i , while it was 1 percent for the ratio R .

Note that this estimator uses ratios of variances and is therefore independent of scale calibration. Also, we can remark that it is not necessary to have pupils of different diameters; the method should work with any DIMM or with a Shack–Hartmann (however, in this case it will not be possible to filter data with the H invariants presented hereafter).

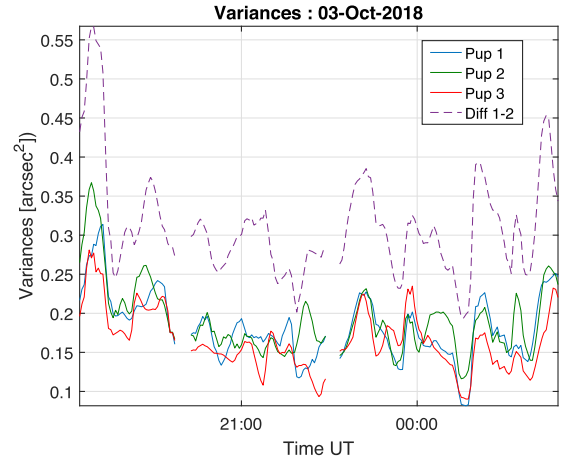


Figure 6. Time series of variances observed at Calern on 2018 October 3. Solid lines: absolute variance in the x direction (declination) for the three sub-pupils. Dashed line: differential longitudinal variance σ_1^2 between pupils 1 and 2. These variances were smoothed by a 10 min large sliding average.

6.1.1 H invariants

Combining equations (1) and (27), we calculated the following ratios:

$$H_t = \frac{\sigma_{D_i}^2 - \sigma_{D_3}^2}{\sigma_t^2} = \frac{0.17(D_1^{-1/3} - D_3^{-1/3})}{0.364D_1^{-1/3} - 0.2905B^{-1/3}}$$

$$H_l = \frac{\sigma_{D_i}^2 - \sigma_{D_3}^2}{\sigma_1^2} = \frac{0.17(D_1^{-1/3} - D_3^{-1/3})}{0.364D_1^{-1/3} - 0.1904B^{-1/3}} \quad (31)$$

where $i = 1, 2$ refers to sub-pupil 1 or 2 (they have the same diameter $D_1 = D_2 = 6$ cm). These ratios appear, at the first order, to be independent of turbulence conditions, so we named them ‘ H invariants’. In fact this invariance is valid for large outer scales ($\mathcal{L}_0/D_i \gg 1$). There is indeed a weak dependence of differential variances $\sigma_{|t}^2$ with the outer scale (Ziad 1993). This dependence is generally omitted in seeing estimations (equations 1 and 2). It can be estimated using equations (5.4) and (5.8) of Conan et al. (2000). For pupils of diameter of 6 cm, the effect of the outer scale on differential variances is under 0.1 per cent for $\mathcal{L}_0 > 10$ m and over 3 per cent for $\mathcal{L}_0 < 1$ m. The impact on H invariants is $\lesssim 0.03$ per cent for $\mathcal{L}_0 > 10$ m and becomes greater than 2 per cent for $\mathcal{L}_0 < 1$ m (these very low outer scales are nevertheless exceptional: at Calern they correspond to less than 0.5 per cent of measured values).

Values of H corresponding to our instrument are

$$H_t = 0.1567 \quad \text{and} \quad H_l = 0.1128. \quad (32)$$

These invariants are easy to calculate and can be used as a filter to reject bad data (contaminated by telescope vibrations). More discussion will be presented in Section 6.2.

6.2 Outer-scale estimation

Estimation of the outer scale requires absolute variances $\sigma_{D_i}^2$ of AA fluctuations for each pupil (in the x direction only). As for differential variances used for seeing estimation, absolute variances are calculated from each image cube, and corrected from exposure time, following the same process as for differential variances (equation 3). One obtains a set of absolute and differential variances

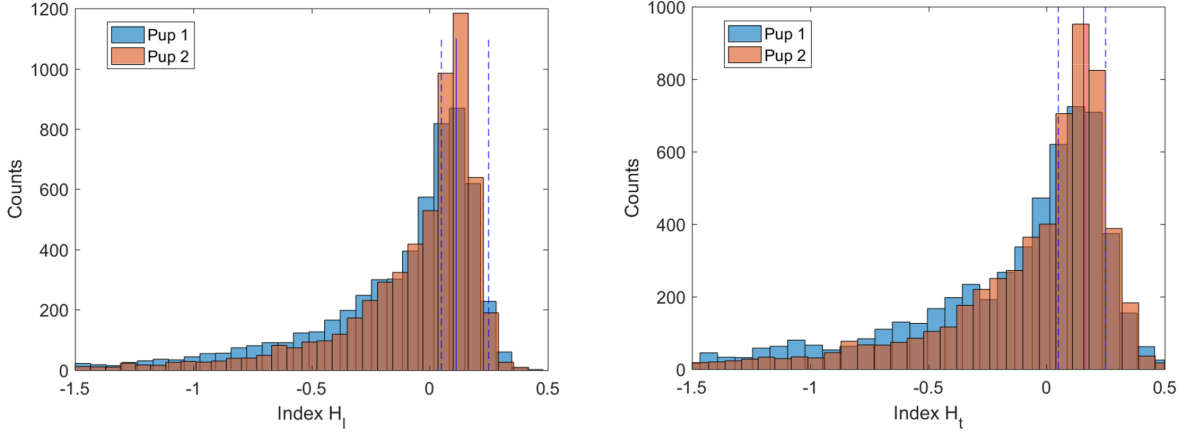


Figure 7. Histograms of invariants H_l (left) and H_t (right) for measured at Calern during the period 2018 August–October. Blue (resp. orange) bars correspond to sub-pupil 1 (resp. 2). The vertical solid line is the theoretical value, and the two dashed lines are rejection thresholds.

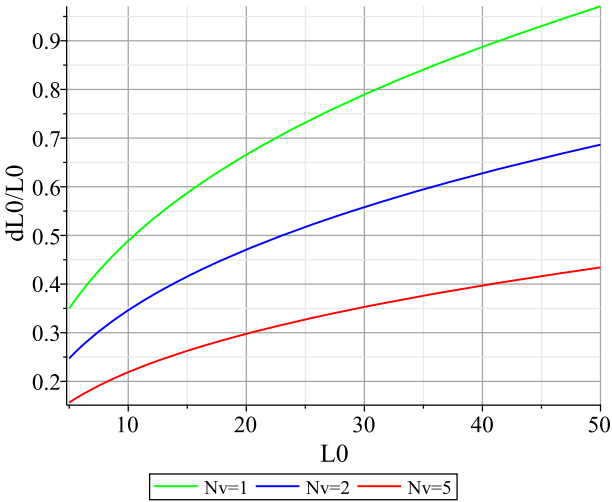


Figure 8. Relative error on \mathcal{L}_0 as a function of \mathcal{L}_0 for different values of N_v (number of averaged variances). The number of images in a sequence is $N = 1024$.

every 2 min. To reduce noise, time series of variances (both absolute and differential) are smoothed by a temporal sliding average. After some trials, the width of the temporal window was set to 10 min, leading to an average of five successive variances, reducing the error by a factor $\sqrt{5}$ (see Section 6.3).

Fig. 6 shows an example of the evolution of these smoothed variances for the night of 2018 October 3. Two things can be noticed on these curves:

(i) The variance $\sigma_{D_3}^2$ corresponding to the sub-pupil 3 should be smallest than $\sigma_{D_1}^2$ according to equation (27). This is not always the case; fluctuations are sometimes larger than the expected difference.

(ii) The differential variance σ_1 between sub-pupils 1 and 2 is almost two times greater than the absolute variances. This is good news: it means that the AA fluctuation signal is not dominated by correlated vibrations due to the telescope mount.

The six ratios Q are calculated from equation (29) leading to six estimations $\mathcal{L}_{0,i}$ of the outer scale. Then, we calculate invariants $H_{l|t}$ (equation 31) to be used as a filter for bad data. Histograms of H invariants obtained during a three-month period (2018 August–October) are displayed in Fig. 7. They present a

peak for the theoretical value ($H_l = 0.1567$ and $H_t = 0.1128$), and somewhat large dispersion around it. This dispersion results mainly from contamination of variances by noise and/or telescope vibrations (there is also a weak contribution due to the dependence of $H_{l|t}$ with the outer scale). After some trials, we decided to reject data for which $H_{l|t} > 0.25$ or $H_{l|t} < 0.05$. That led to rejection of about 70 percent of the individual outer scales $\mathcal{L}_{0,i}$. The final outer-scale value is the median of the remaining $\mathcal{L}_{0,i}$ after filtering.

6.3 Error analysis

The estimation of \mathcal{L}_0 is made from the ratios Q_i by inverting equation (30). The error δ_Q comes from errors on variances that propagate to Q_i via equation (29).

To increase accuracy, we perform a rolling average of measured variances (they are calculated every 2 min) over time intervals of T (set to $T = 10$ min), corresponding to an average of $N_v = 5$ individual variances, thus reducing the error by $\sqrt{N_v}$ on variances. The relative error δ_Q on Q_i is expressed as

$$\frac{\delta_Q}{Q_i} = \frac{1}{\sqrt{N_v}} \left(\frac{\delta\sigma_{D_i}^2}{\sigma_{D_i}^2} + \frac{\delta\sigma_{l|t}^2}{\sigma_{l|t}^2} \right). \quad (33)$$

Taking only the statistical error on variances (they do indeed dominate, as discussed in Section 3.2.1), we obtain $\frac{\delta_Q}{Q_i} \simeq 5$ per cent for $N = 1024$ images and $N_v = 5$. The error $\delta\mathcal{L}_0$ on the outer scale is obtained by the finite difference

$$\delta\mathcal{L}_0 = \mathcal{L}'_0(Q_i) \delta_Q \quad (34)$$

where the derivative $\mathcal{L}'_0(Q_i)$ is calculated from equation (30). The expected relative error $\frac{\delta\mathcal{L}_0}{\mathcal{L}_0}$ (due to the statistical error) is shown in Fig. 8. Three curves are plotted for different values of N_v in the range $\mathcal{L}_0 \in [5, 50]$ m. Both show that low \mathcal{L}_0 values are estimated with better precision. With $N_v = 1$ (no variance averaging) it is impossible to obtain reliable values of \mathcal{L}_0 (relative error is ~ 70 per cent for $\mathcal{L}_0 = 20$ m). An average of at least $N_v = 5$ individual variances is necessary to obtain acceptable error bars ($\frac{\delta\mathcal{L}_0}{\mathcal{L}_0} \simeq 30$ per cent for $\mathcal{L}_0 = 20$ m). The drawback is that one obtains estimations of \mathcal{L}_0 smoothed over time intervals 10 min with $N_v = 5$. This is greater than the characteristic time of outer-scale fluctuations, whose value, estimated by GSM, is of the order of 6 min (Ziad 2016).

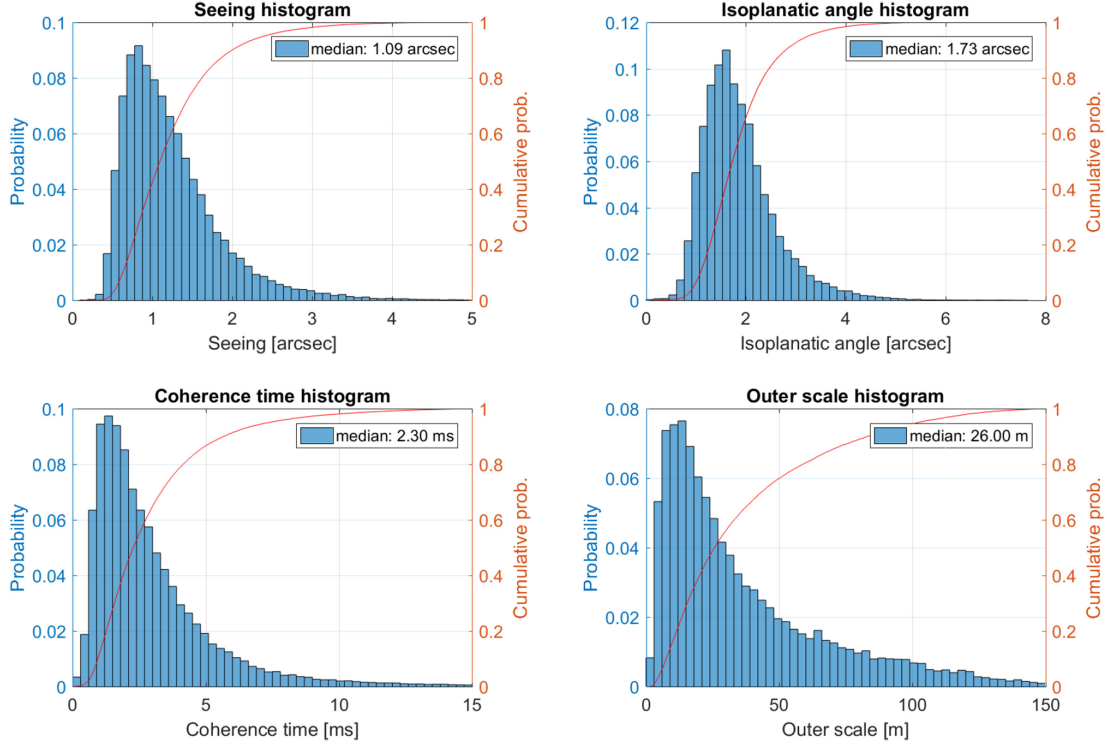


Figure 9. Histograms of turbulence parameters at Calern, calculated at the wavelength $\lambda = 0.5 \mu\text{m}$.

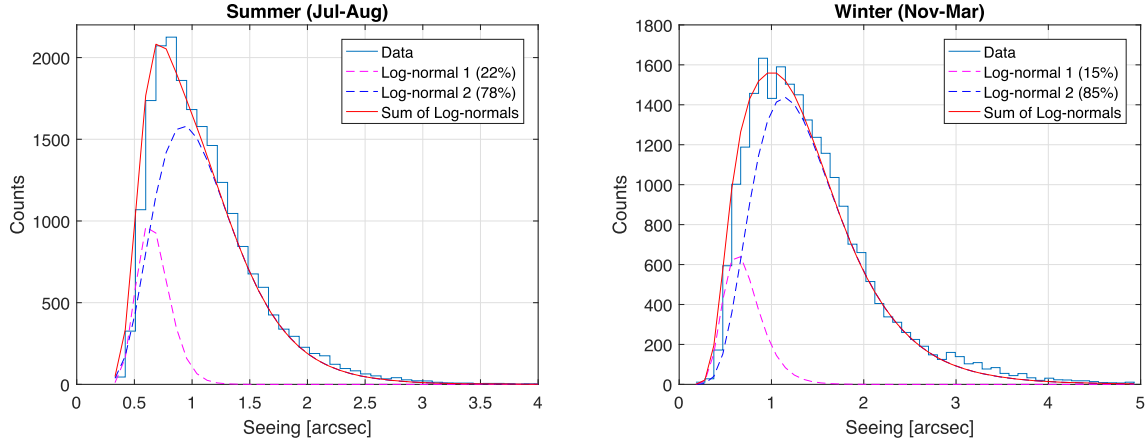


Figure 10. Left: seeing histogram for the summer (July–August). Right: seeing histogram for the winter (Nov–March). Superimposed curves are a least-squares fit by a sum of two lognormal distributions (individual lognormal curves are dashed lines). The percentages corresponding to each lognormal distribution are indicated in the legend.

The statistical error is not the only contribution to the total uncertainty, especially for absolute variances that are contaminated by vibrations. A measure of their effect on \mathcal{L}_0 can be made from the remaining distribution of H invariants after filtering (see Section 6.2). The thresholds on $H_{|t}$ to filter the data were obtained as a trade-off between data quality and the number of variances kept for outer-scale estimation. The remaining H distribution has a dispersion $\Delta H \simeq 0.1$ around the nominal value. This results in an error $\Delta \mathcal{L}_0$ on the outer scale. To estimate it, we rewrite equation (31) as

$$H_{|t} = Q_{i,|t} - Q_{3,|t} \quad (35)$$

so that

$$\Delta H \simeq \Delta Q_{i,|t} + \Delta Q_{3,|t} \simeq 0.1 \quad (36)$$

corresponding to an uncertainty $\Delta Q_{i,|t} \simeq 0.05$ on the ratios Q . Writing

$$\Delta Q_{i,|t} = \frac{\partial Q_{i,|t}}{\partial \mathcal{L}_0} \Delta \mathcal{L}_0 \quad (37)$$

and making use of equation (30) to calculate $\frac{\partial Q_{i,|t}}{\partial \mathcal{L}_0}$, we found that the resulting relative error on \mathcal{L}_0 is of the order of 50 per cent for \mathcal{L}_0 around 20m.

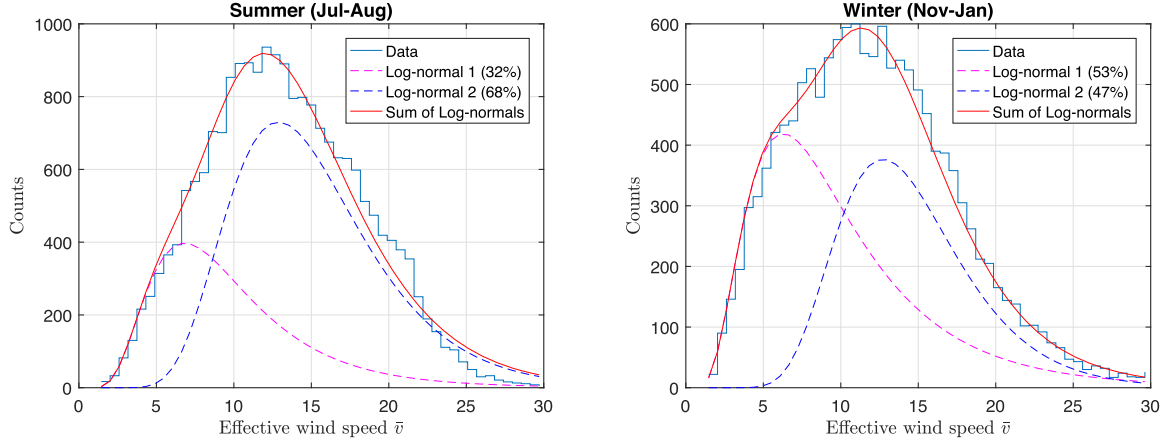


Figure 11. Histograms of the effective wind speed in winter (November–January). Superimposed curves are a least-squares fit by a sum of two lognormal distributions. Left: summer histogram. Right: winter histogram.

Table 3. Statistics of turbulence parameters measured at Calern (at the wavelength $\lambda = 0.5 \mu\text{m}$) during the period 2015 June–2018 October. Paranal, La Silla and Mauna Kea values are from the GSM database.

	ϵ_0 [arcsec]	θ_0 [arcsec]	τ_0 [ms]	\mathcal{L}_0 [m]	\bar{h} [m]	\bar{v} [m s $^{-1}$]
Median	1.09	1.73	2.30	26.00	3436	12.84
Mean	1.23	1.86	3.10	37.14	3698	13.59
Std. dev.	0.52	0.65	1.80	29.20	1566	5.47
1st quartile	0.80	1.35	1.40	13.50	2504	9.24
3rd quartile	1.49	2.21	3.80	51.00	4618	16.74
1st centile	0.45	0.58	0.50	3.10	1121	3.03
Last centile	3.37	4.27	14.90	142.25	10279	30.23
Paranal	0.81	2.45	2.24	22	3256	17.3
La Silla	1.64	1.25	1.46	25.5	3152	13.1
Mauna Kea	0.75	2.94	2.43	24	2931	17.2

We are currently working on improvements to the algorithm of \mathcal{L}_0 calculation to find better metrics and to reduce the effect of vibrations, an issue with small telescopes.

7 FIRST LONG-TERM GDIMM STATISTICS

A total of 70 097 turbulence parameter measurements (22 698 for \mathcal{L}_0) were collected at Calern observatory during the 3.5 yr period from 2015 June to 2018 October. Half of the data were obtained during the summer season (June to September) when meteorological conditions are better. Statistics are presented in Table 3 for the four turbulence parameters (ϵ_0 , θ_0 , τ_0 , \mathcal{L}_0) and for the equivalent turbulence altitude (equation 8) and the effective wind speed (equation 16). Histograms are displayed in Fig. 9 and show a classical lognormal shape for all parameters. Comparisons with other astronomical sites in the world (examples for Paranal, La Silla and Mauna Kea are given in Table 3) show that the Calern plateau is an average site.

The seeing is slightly lower in summer; we measured a median value of 0.96 arcsec in July and August (the median winter seeing during the period November–January is 1.21 arcsec). As a consequence, the median coherence time is higher in summer (3.2 ms in July–August, 2.40 ms in November–January). The outer scale \mathcal{L}_0 has values similar to other sites such as Mauna Kea or La Silla.

Sequences of several hours of good seeing were sometimes observed, which is a good point for this site (and already known by ‘old’ observers on interferometers during the 1980s and 1990s). Fig. 10 displays seasonal seeing histograms, calculated for the summer (July and August) and the winter (November–March). They appear to be well modelled by a sum of two lognormal functions (they appear as dashed curves on the plots; their sum is the solid line). This is evidence of the existence of two regimes: a ‘good seeing’ distribution with a median value ϵ_1 and a ‘medium seeing’ situation with a median value ϵ_2 . In summer, we have $\epsilon_1 = 0.63$ arcsec (the good seeing distribution contains 22 per cent of the data) and $\epsilon_2 = 0.95$ arcsec (78 per cent of the data). In winter we have $\epsilon_1 = 0.66$ arcsec (15 per cent of the data) and $\epsilon_2 = 1.15$ arcsec (85 per cent of the data).

The equivalent turbulence altitude \bar{h} has a median value around 3 km, which is comparable to other classical sites. However, we noticed a difference between the summer and the winter. During the two months of July and August, the median value of \bar{h} was 3940 m, while it is only 2870 m in winter (November to March). Situations with a high value of \bar{h} correspond to less turbulence in the ground layer, giving good seeing conditions as the ground layer is the main contributor to the total seeing.

As for the seeing, the effective wind speed histograms (Fig. 11) are bimodal and can be modelled by the sum of two lognormal functions. They peak at $\bar{v}_1 = 6.7 \text{ m s}^{-1}$ and $\bar{v}_2 = 13 \text{ m s}^{-1}$ for both the summer and the winter. They contain respectively 32 per cent and 68 per cent of the data in summer; these proportions go to 53 per cent and 47 per cent in winter. The value $\bar{v}_1 = 6.7 \text{ m s}^{-1}$ is indeed close to the median ground wind speed $v_G = 5.7 \text{ m s}^{-1}$ measured by the meteorological station.

8 CONCLUSIONS

We have presented the GDIMM, a new turbulence monitor aiming to measure the four integrated parameters of optical turbulence. The GDIMM is a small instrument, easy to transport to make measurements at any site in the world, and was designed to provide monitoring of the four integrated parameters of atmospheric turbulence, i.e. seeing, isoplanatic angle, coherence time and outer scale.

Seeing measurements are given by differential motion, according to a well established theory and to an instrumental concept that

makes them robust to telescope vibrations (Sarazin & Roddier 1990; Vernin & Munoz-Tunon 1995). Isoplanatic angle measurements are made via scintillation, again following a well known technique (Loos & Hogge 1979), which has become popular thanks to its simplicity. It appears to give satisfactory results when compared to other techniques (Ziad et al. 2018a). We indeed used these two techniques intensively to measure ϵ_0 and θ_0 during the campaigns of site testing of the site of Dome C in Antarctica (see Aristidi 2012 and references therein).

The method for estimating the coherence time from the decorrelation time of AA fluctuations is recent. It was proposed a few years ago (Ziad et al. 2012) and is based upon analytical developments by Conan et al. (2000). First tests on reprocessed GSM data and comparisons with radio soundings (Ziad et al. 2012) showed the pertinence of the method. The instrumental concept is simple, compared to other monitors such as the Multi-Aperture Scintillation Sensor (MASS-DIMM, Kornilov et al. 2007); the only requirement is to have a camera allowing a high frame rate (at least 100 frames per second) to properly sample the AA decorrelation time. After GSM in the past, the GDIMM is now, to our knowledge, the first monitor to use this method routinely to calculate τ_0 . A true asset of the GDIMM is the possibility of measuring the outer scale. In particular, obtaining reliable values of \mathcal{L}_0 is a challenge with small instruments, and this parameter is often neglected, though it has a strong impact on high angular resolution techniques, especially for extremely large telescopes (see the recent review by Ziad 2016). We have proposed here a method based on the ratios of absolute to differential motions. It is simple and can work with any DIMM or Shack–Hartmann-based monitor, but requires good stability of the telescope mount since it is sensitive to vibrations.

A portable version of the GDIMM has been developed in parallel with the Calern one, to perform turbulence measurements at any site in the world. Discussions with the ESO (European Southern Observatory) are currently in progress to make GDIMM and PML observations at Paranal and compare them with the ESO Astronomical Site Monitor (Chiozzi et al. 2016).

ACKNOWLEDGEMENTS

We would like to thank Jean-Marie Torre and Hervé Viot, from the Calern technical staff, for their valuable help with the electronics of the instrument. Thanks also to M. Marjani who worked on our data during his master thesis. The CATS project has been done under the financial support of CNES, Observatoire de la Côte d’Azur, Labex First TF, AS-GRAM, Federation Doblin, Université de Nice-Sophia Antipolis and Région Provence Alpes Côte d’Azur.

REFERENCES

- Aristidi E., 2012, in Boissier S., de Laverny P., Nardetto N., Samadi R., Valls-Gabaud D., Wozniak H., eds, SF2A-2012: Proceedings of the annual meeting of the French society of astronomy and astrophysics, p. 697
- Aristidi E., Fantei-Caujolle Y., Ziad A., Dimur C., Chabé J., Roland B., 2014, in SPIE Conference Series on Ground-based and Airborne Telescopes V, vol. 9145, p. 91453G
- Aristidi E., Fantei-Caujolle Y., Chabé J., Renaud C., Ziad A., Ben Rahhal M., 2018, in SPIE Conference Series on Astronomical Telescopes+Instrumentation, Austin, Texas, vol. 10703, p. 107036U
- Bendjoya P., Abe L., Rivet J.-P., Suárez O., Vernet D., Mékarnia D., 2012, in Boissier S., de Laverny P., Nardetto N., Samadi R., Valls-Gabaud D., Wozniak H., eds, SF2A-2012: Proceedings of the annual meeting of the French society of astronomy and astrophysics, p. 643
- Carbillet M., Aristidi E., Giordano C., Vernin J., 2017, *MNRAS*, 471, 3043
- Chiozzi G., Sommer H., Sarazin M., Bierwirth T., Dorigo D., Vera Sequeiros I., Navarrete J., Del Valle D., 2016, in SPIE Conference Series on Software and Cyberinfrastructure for Astronomy IV, vol. 9913, p. 991314
- Conan R., Borgnino J., Ziad A., Martin F., 2000, *J. Opt. Soc. America A*, 17, 1807
- Frieden B. R., 1983, *Probability, Statistical Optics, and Data Testing*. Springer, Berlin
- Kornilov V., Tokovinin A., Shatsky N., Voziakova O., Potanin S., Safonov B., 2007, *MNRAS*, 382, 1268
- Labeyrie A., 1970, *A&A*, 6, 85
- Labeyrie A., 1975, *ApJ*, 196, L71
- Loos G., Hogge C., 1979, *Appl. Opt.*, 18, 15
- Roddier F., 1981, *Progress Opt.*, 19, 281
- Roddier F., Gilli J. M., Vernin J., 1982, *J. Opt.*, 13, 63
- Rousset G., Fontanella J. C., Kern P., Gigan P., Rigaut F., 1990, *A&A*, 230, L29
- Samain E. et al., 2008, in 16th International Workshop on Laser Ranging, p. 88
- Sarazin M., Roddier F., 1990, *A&A*, 227, 294
- Tokovinin A., 2002, *PASP*, 114, 1156
- Vernin J., Munoz-Tunon C., 1995, *PASP*, 107, 265
- Winker D. M., 1991, *J. Opt. Soc. America A*, 8, 1568
- Ziad A., 1993, PhD thesis, Université de Nice – Sophia Antipolis, France
- Ziad A., 2016, in SPIE Conference Series on Adaptive Optics Systems V, vol. 9909, p. 99091K
- Ziad A., Borgnino J., Martin F., Agabi A., 1994, *A&A*, 282, 1021
- Ziad A., Conan R., Tokovinin A., Martin F., Borgnino J., 2000, *Appl. Opt.*, 39, 5415
- Ziad A., Borgnino J., Dali Ali W., Berdja A., Maire J., Martin F., 2012, *J. Opt.*, 14, 045705
- Ziad A. et al., 2017, in *Adaptive Optics for Extremely Large Telescopes AO4ELT 5*, p. 25
- Ziad A., Aristidi E., Chabé J., Borgnino J., 2018a, *MNRAS*, submitted
- Ziad A., Chabé J., Fantei-Caujolle Y., Aristidi E., Renaud C., Ben Rahhal M., 2018b, in SPIE Conference Series on Adaptive Optics Systems VI, vol.10703, p. 107036L

This paper has been typeset from a $\text{\TeX}/\text{\LaTeX}$ file prepared by the author.